A kinetic method for solving the MHD equations. Application to the computation of tilt instability on uniform fine meshes.

Hubert Baty[1], Florence Drui[2], Emmanuel Franck[3], Philippe Helluy[3], Christian Klingenberg[4], and Lukas Tannhaüser[4]

Abstract This paper is devoted to the simulation of MHD flows with complex structures. This kind flows present instabilities that generate shock waves. We propose a robust and precise numerical method based on the Lattice Boltzmann methodology. We explain how to adjust the numerical viscosity in order to obtain stable, precise results and reduced divergence errors. This method can handle shock wave and is almost second order. It is also very well adapted to GPU computing. We also give results for a tilt instability test case on very fine meshes.

1 Introduction

The MagnetoHydroDynamic (MHD) system is a fundamental model used in many fields of physics: astrophysics, plasma physics, geophysics... Indeed, the MHD model is commonly adopted as an excellent framework for collisional plasma environments. The numerical approximation of this system is a difficult task. Compared to other models in fluid mechanics, it contains more conservative unknowns and thus more scales and more different wave speeds. It is also subject to complex phenomena such as occurrence of shock waves, current sheet formation, magnetic reconnection, instabilities and turbulent behaviors. An additional specificity is that the magnetic field has to satisfy a free divergence condition, which generally difficult to be verified by numerical solutions. In order to deal with the divergence-free condition, we adopt here a modified version of the MHD equations by a divergence cleaning term proposed in [13].

We propose a simple scheme, based on an abstract kinetic interpretation, for computing two-dimensional MHD solutions. The kinetic interpretation is

Observatoire de Strasbourg · CEA Saclay · IRMA Université de Strasbourg Inria Tonus
philippe.helluy@unistra.fr · University of Würzburg

vectorial and has been first proposed by Bouchut in [6] and Aregba-Natalini in [1]. In this approach, the original system of conservation laws is represented by a system of transport equations coupled through a so-called collision source term. The idea originates from the Boltzmann kinetic theory of gases, but it is purely abstract and has no physical meaning. It leads to natural numerical methods, where the transport step and the collision step are made separately. Other interesting features arise from this representation (see [2, 10], for instance).

In this paper, we solve the kinetic representation with a Lattice-Boltzmann Method (LBM), where the resolution of the transport step is done exactly on a regular grid. An important aspect of the LBM is the choice of the relaxation parameter in the collision step. The choice of the parameter allows adjusting the numerical viscosity of the LBM scheme. We provide a analysis in a simplified one-dimensional framework which shows that it is possible to adjust more precisely the numerical viscosity with a generalized matrix relaxation parameter. We also show that the divergence cleaning effect is improved if the relaxation parameter is chosen differently for the physical variables and the divergence cleaning potential.

In order to capture fine structures, it is necessary to consider very fine meshes. We have programmed the algorithm in a very efficient way in order to address recent GPUs (Graphic Purpose Units) or multicore CPUs. We describe the implementation, which relies on OpenCL and PyOpenCL, and the memory optimizations used for reaching high performance. The program allows performing full MHD simulations on grids as fine as 7000×7000 within a few hours.

Finally, we apply the whole approach to several MHD simulations: the classical Orszag-Tang test and a more physical study of ideal MHD instabilities (tilt modes) and associated formation of quasi-singular current sheets.

2 Mathematical model

2.1 MHD equations with divergence cleaning

We consider the MHD equations with Divergence Cleaning [13] (called the MHD-DC equations in the following)

$$\partial_t \begin{pmatrix} \rho \\ \rho\mathbf{u} \\ Q \\ \mathbf{B} \\ \psi \end{pmatrix} + \nabla\cdot \begin{pmatrix} \rho\mathbf{u} \\ \rho\mathbf{u}\otimes\mathbf{u} + (p + \frac{\mathbf{B}\cdot\mathbf{B}}{2})\mathbf{I} - \mathbf{B}\otimes\mathbf{B} \\ (Q + p + \frac{\mathbf{B}\cdot\mathbf{B}}{2})\mathbf{u} - (\mathbf{B}\cdot\mathbf{u})\mathbf{B} \\ \mathbf{u}\otimes\mathbf{B} - \mathbf{B}\otimes\mathbf{u} + \psi\mathbf{I} \\ c_h^2\mathbf{B} \end{pmatrix} = \begin{pmatrix} 0 \\ 0 \\ 0 \\ 0 \\ 0 \end{pmatrix}.$$

The velocity and magnetic field are noted

$$\mathbf{u}=(u_1,u_2,u_3)^T, \quad \mathbf{B}=(B_1,B_2,B_3)^T,$$

the pressure is defined by

$$p=(\gamma-1)(Q-\rho\frac{\mathbf{u}\cdot\mathbf{u}}{2}-\frac{\mathbf{B}\cdot\mathbf{B}}{2}).$$

The other variables are the density ρ, the total energy Q, the divergence cleaning potential ψ. The velocity is a positive parameter $c_h>0$.

When the magnetic field satisfies the divergence-free condition

$$\nabla\cdot\mathbf{B}=0,$$

and the potential ψ is a constant, then the MHD-DC equations simply reduce to the usual MHD equations. In other words, MHD-DC equations are a generalization of the MHD equations, where the magnetic field can have a non-vanishing divergence. The interest of this formulation is for numerical approximations. Indeed, standard approximations of the usual MHD equations suffer from drifting errors along time of the divergence constraint [28, 13, 4]. Approximations of the MHD-DC generally have a much better behavior. In this generalized model, the divergence errors propagate at the wave speed c_h. The errors are then damped at the boundaries of the computational domain.

Theoretically, the parameter c_h can take any value. But in practice it is generally chosen larger than all the wave speeds of the MHD system (see [13]).

We introduce the conservative variables

$$\mathbf{w}=\mathbf{w}(\mathbf{x},t)=\begin{pmatrix}\rho\\ \rho\mathbf{u}\\ Q\\ \mathbf{B}\\ \psi\end{pmatrix}\in\mathbb{R}^m, \quad m=9.$$

and the flux ($\mathbf{n}$ is a vector of $\mathbb{R}^3$)

$$\mathbf{F}(\mathbf{w},\mathbf{n})=\begin{pmatrix}\rho\mathbf{u}\cdot\mathbf{n}\\ \rho\mathbf{u}\cdot\mathbf{n}\mathbf{u}+(p+\frac{\mathbf{B}\cdot\mathbf{B}}{2})\mathbf{n}-\mathbf{B}\cdot\mathbf{n}\mathbf{B}\\ (Q+p+\frac{\mathbf{B}\cdot\mathbf{B}}{2})\mathbf{u}\cdot\mathbf{n}-(\mathbf{B}\cdot\mathbf{u})\mathbf{B}\cdot\mathbf{n}\\ \mathbf{u}\cdot\mathbf{n}\mathbf{B}-\mathbf{B}\cdot\mathbf{n}\mathbf{u}+\psi\mathbf{n}\\ c_h^2\mathbf{B}\cdot\mathbf{n}\end{pmatrix}\in\mathbb{R}^m.$$

In this work, we assume that all the fields do not depend on the x_3 space variable. We are thus computing two-dimensional solutions. If we set

$$\mathbf{n}_1=(1,0,0)^T, \quad \mathbf{n}_2=(0,1,0)^T, \quad \mathbf{F}_1=\mathbf{F}(\mathbf{w},\mathbf{n}_1), \quad \mathbf{F}_2=\mathbf{F}(\mathbf{w},\mathbf{n}_2),$$

the MHD equations can also be written as a two-dimensional system of nine conservation laws

$$\partial_t \mathbf{w} + \partial_1 \mathbf{F}_1 + \partial_2 \mathbf{F}_2 = 0, \tag{1}$$

where we use the notation ∂_i for the partial derivative $\partial/\partial x_i$. If the fields depend only on the x_1 space variable, the system reduces to

$$\partial_t \mathbf{w} + \partial_1 \mathbf{F}_1 = 0. \tag{2}$$

In this case, the mathematical analysis is simplified. We shall perform an analysis of the numerical viscosity of the kinetic method in this simplified framework.

3 Kinetic representation

The Lattice-Boltzmann Method (LBM) originated from the physical kinetic interpretation of the Navier-Stokes equations [8]. In the physical world, the fluid particles can have arbitrary velocities. The main idea of the LBM is that it is possible to construct abstract kinetic interpretations of the Navier-Stokes equations in which the particles velocities can take a few number of given values. This makes it possible to solve the kinetic model directly in an efficient way. We refer to [31] for a history of the LBM. Initially devised for solving Navier-Stokes equations, the LBM has more recently been extended to any systems of conservation laws. For more generality, it is necessary to accept vectorial kinetic distribution functions instead of only scalar ones [6, 1, 14, 20]. It is now possible to approximate any systems of conservation laws with minimal lattice vectorial kinetic model. This approach is very fruitful and can be used on arbitrary unstructured meshes at any order of approximation [3, 9]. In addition, when the lattice velocities are aligned with the mesh, it is possible to adopt a very simple exact solver of the transport step. This is the method that we present here.

We consider a real number $\lambda > 0$ and four velocities $\mathbf{v}_k = (v_k^1, v_k^2)^T$, $k = 1 \ldots 4$, defined by

$$\mathbf{v}_1 = \begin{pmatrix} -\lambda \\ 0 \end{pmatrix}, \quad \mathbf{v}_2 = \begin{pmatrix} \lambda \\ 0 \end{pmatrix}, \quad \mathbf{v}_3 = \begin{pmatrix} 0 \\ -\lambda \end{pmatrix}, \quad \mathbf{v}_4 = \begin{pmatrix} 0 \\ \lambda \end{pmatrix}.$$

We have four vectorial distribution functions $\mathbf{f}_k(\mathbf{x}, t) \in \mathbb{R}^m$, $k = 1 \ldots 4$. The conservative variable $\mathbf{w}$ is related to the kinetic data by

$$\mathbf{w} = \sum_{k=1}^{4} \mathbf{f}_k.$$

Usually, in the Lattice-Boltzmann philosophy, the kinetic system is a set a transport equations coupled through a relaxation source term and reads (with $\tau > 0$)

$$\partial_t \mathbf{f}_k + \mathbf{v}_k \cdot \nabla \mathbf{f}_k = \boldsymbol{\mu}_k = \frac{1}{\tau}(\mathbf{f}_k^{eq} - \mathbf{f}_k), \quad k = 1 \dots 4. \tag{3}$$

The equilibrium function $\mathbf{f}_k^{eq}$ also called the Maxwellian state is chosen as

$$\mathbf{f}_1^{eq}(\mathbf{w}) = \frac{1}{4}\mathbf{w} - \frac{1}{2\lambda}\mathbf{F}_1(\mathbf{w}), \quad \mathbf{f}_2^{eq}(\mathbf{w}) = \frac{1}{4}\mathbf{w} + \frac{1}{2\lambda}\mathbf{F}_1(\mathbf{w}),$$

$$\mathbf{f}_3^{eq}(\mathbf{w}) = \frac{1}{4}\mathbf{w} - \frac{1}{2\lambda}\mathbf{F}_2(\mathbf{w}), \quad \mathbf{f}_4^{eq}(\mathbf{w}) = \frac{1}{4}\mathbf{w} + \frac{1}{2\lambda}\mathbf{F}_2(\mathbf{w}).$$

One can check that

$$\mathbf{w} = \sum_{k=1}^{4} \mathbf{f}_k^{eq}, \quad \mathbf{F}_i = \sum_{k=1}^{4} v_k^i \mathbf{f}_k^{eq}. \tag{4}$$

When the relaxation time $\tau \to 0$ then from (3) we see that

$$\mathbf{f}_k \simeq \mathbf{f}_k^{eq},$$

and thus from (4) we recover the MHD equations (1).

But in practice, it is quite difficult to solve directly equation (3) because the relaxation source term couples all the kinetic transport equation. It is better to replace the source term in such a way that most of the time it vanishes and thus the coupling is limited. For this, we introduce the Dirac comb Ψ defined by

$$\Psi(t) = \sum_{i \in \mathbb{Z}} \delta(t - i\Delta t),$$

where δ is the usual Dirac measure and Δt a positive time step. Let ω be a relaxation parameter $\in [1, 2]$. The source term is then written as

$$\boldsymbol{\mu}_k(\mathbf{x}, t) = \omega \Psi(t) \left(\mathbf{f}_k^{eq}(\mathbf{w}(\mathbf{x}, t^-)) - \mathbf{f}_k(\mathbf{x}, t^-) \right).$$

In other words, at times $t = i\Delta t$, $\mathbf{f}$ has jumps in time and the values after the jump

$$\mathbf{f}_k(\mathbf{x}, t^+) = \mathbf{f}_k(\mathbf{x}, t^-) + \omega \left(\mathbf{f}_k^{eq}(\mathbf{w}(\mathbf{x}, t^-)) - \mathbf{f}_k(\mathbf{x}, t^-) \right).$$

This comes from the definition of the time derivative in the weak sense. The computation of the jumps at times $t = i\Delta t$ are called the collision steps.

The rest of the time, $\mathbf{f}_k$ is solution of the free transport equation

$$\partial_t \mathbf{f}_k + \mathbf{v}_k \cdot \nabla \mathbf{f}_k = 0.$$

The coupling indeed occurs only at times $t = i\Delta t$.

Let us remark that when $\omega = 1$ the collision step reads

$$\mathbf{f}_k(\mathbf{x}, t^+) = \mathbf{f}_k^{eq}(\mathbf{w}(\mathbf{x}, t^-)).$$

It is a simple projection on the Maxwellian state associated to the conservative data. This scheme is a first order in time approximation of the original equations. An interesting case is the case of over-relaxation $\omega = 2$. Then the scheme is a second order in time approximation of the original equations. See for instance [15]). See also below for a mathematical analysis in the one-dimensional case.

4 Numerical method

For solving (3) numerically, we first construct a regular grid of the square

$$\mathcal{D} =]0, L[\times]0, L[.$$

The space step

$$\Delta x = \frac{L}{N}.$$

Grid points

$$\mathbf{x}_{i,j} = \begin{pmatrix} (i + \frac{1}{2})\Delta x \\ (j + \frac{1}{2})\Delta x \end{pmatrix}, \quad i, j \in \frac{\mathbb{Z}}{N\mathbb{Z}}.$$

We assume periodic conditions, therefore

$$i + N = i, \quad j + N = j.$$

We denote by $\mathbf{w}_{i,j}^n$ and $\mathbf{f}_{k,i,j}^n$ the approximation of $\mathbf{w}$ and $\mathbf{f}_k$ at the grid points $\mathbf{x}_{i,j}$ and time $t_n = n\Delta t$ just after the collision step. The values of the kinetic vectors just before the collision step are noted $\mathbf{f}_{k,i,j}^{n,-}$. For solving the kinetic system (3) we treat separately the transport and the relaxation terms.

4.1 Transport solver

The characteristic method gives

$$\mathbf{f}_k(\mathbf{x}, t + \Delta t) = \mathbf{f}_k(\mathbf{x} - \Delta t \mathbf{v}_k, t).$$

We use the following notation for the transport operator

$$\mathbf{f}(\mathbf{x}, t + \Delta t) = \mathbf{T}(\Delta t)\mathbf{f}(\mathbf{x}, t).$$

If we assume that the time step satisfies

$$\Delta t = \frac{\Delta x}{\lambda},$$

the transport operator then reduces to a simple shift. Before the collision step, we have thus

$$\mathbf{f}_{1,i,j}^{n+1,-} = \mathbf{f}_{1,i+1,j}^{n}, \quad \mathbf{f}_{2,i,j}^{n+1,-} = \mathbf{f}_{2,i-1,j}^{n}, \quad \mathbf{f}_{3,i,j}^{n+1,-} = \mathbf{f}_{3,i,j+1}^{n}, \quad \mathbf{f}_{4,i,j}^{n+1,-} = \mathbf{f}_{4,i,j-1}^{n}. \tag{5}$$

4.2 Relaxation

At the end of the transport step, we can compute the conservative data

$$\mathbf{w}_{i,j}^{n+1} = \sum_{k=1}^{4} \mathbf{f}_{k,i,j}^{n+1,-}. \tag{6}$$

The usual projection method would be to write

$$\mathbf{f}_{k,i,j}^{n+1} = \mathbf{f}_{k}^{eq}(\mathbf{w}_{i,j}^{n+1}). \tag{7}$$

As stated above, it is more precise to consider an over-relaxation

$$\mathbf{f}_{k,i,j}^{n+1} = 2\mathbf{f}_{k}^{eq}(\mathbf{w}_{i,j}^{n+1}) - \mathbf{f}_{k,i,j}^{n+1,-}.$$

It is possible to add a small dissipation $\tau > 0$. See [20] or [9] for the relaxation scheme in the case $\tau > 0$. This dissipation provides a better stability in numerical cases, when sharp fronts are generated.

The relaxation step finally reads

$$\mathbf{f}_{k,i,j}^{n+1} = \omega \mathbf{f}_{k}^{eq}(\mathbf{w}_{i,j}^{n+1}) - (\omega - 1)\mathbf{f}_{k,i,j}^{n+1,-}, \tag{8}$$

where $\omega = \frac{2\Delta t}{2\tau + \Delta t}$. Typically, one will choose $\omega = 1.9$ in our simulations.

4.3 Boundary conditions

For the moment, we have assumed periodic boundary conditions. But Dirichlet or Neumann conditions are also possible. Neumann conditions are a good candidate for handling variables associated with outgoing waves. Indeed, because of the hyperbolic nature of the equations, it is not possible to impose all the physical data at the boundaries. The number of boundary conditions depends on the wave pattern. We refer to [16], for a specific analysis of the boundary conditions in the over-relaxation scheme.

5 Analysis of the numerical viscosity in the one-dimensional case

In this section, we state some results about the numerical viscosity of the kinetic relaxation scheme in the one-dimensional case. This one-dimensional analysis will give us simple intuitions for adjusting the relaxation parameter in the 2D case. We consider the one-dimensional MHD-DC system (2). For more simplicity, we will note $\mathbf{F} = \mathbf{F}_1$ and $x = x_1$. The equations then read

$$\partial_t \mathbf{w} + \partial_x \mathbf{F}(\mathbf{w}) = 0$$

For the analysis, it is possible to replace the scalar relaxation parameter ω by a matrix $\boldsymbol{\Omega}$, for more generality. In the following, we understand the comparison of matrices in the usual way, by the comparison of the associated quadratic form (the resulting order is thus not total).

It is then possible to prove the following result:

Theorem 1 *If the relaxation matrix satisfies* $\mathbf{I} < \boldsymbol{\Omega} < 2\mathbf{I}$ *and if* $\mathbf{f} = \mathbf{f}^{eq}$ *at the initial time, then, up to second-order terms in* $O(\Delta t^2)$*,* $\mathbf{w}$ *is a solution of the following system of conservation laws*

$$\partial_t \mathbf{w} + \partial_x \mathbf{F}(\mathbf{w}) = \lambda^2 \Delta t \partial_x \left((\boldsymbol{\Omega}^{-1} - \frac{1}{2}\mathbf{I})(\mathbf{I} - \frac{1}{\lambda^2}\mathbf{F}'(\mathbf{w})^2)\partial_x \mathbf{w} \right) + O(\Delta t^2).$$

Remark 1 The proof is based on standard Taylor expansions. For the scalar case $\boldsymbol{\Omega} = \omega \mathbf{I}$, it can be found in [11]. The approach is classical in the analysis of the Lattice Boltzmann Method (LBM). See for instance [17, 26].

The above analysis allows recovering formally the so-called sub-characteristic condition. Assuming that $\mathbf{I} < \boldsymbol{\Omega} < 2\mathbf{I}$, the second-order ("viscous") terms have the good sign, which ensures stability of the model, if the following matrix is positive:

$$\mathbf{V}(\lambda, \mathbf{w}) = \mathbf{I} - \frac{1}{\lambda^2}\mathbf{F}'(\mathbf{w})^2 > 0. \tag{9}$$

We also recover the fact that the scheme is second-order in time in the over-relaxation case, when

$$\boldsymbol{\Omega} = 2\mathbf{I}.$$

Finally, this analysis provides a way to numerically approximate, up to second order in time the second-order system of conservation laws

$$\partial_t \mathbf{w} + \partial_x \mathbf{F}(\mathbf{w}) - \partial_x \left(\mathbf{A}(\mathbf{w})\partial_x \mathbf{w}\right) = 0. \tag{10}$$

If the diffusion matrix $\mathbf{A}(\mathbf{w})$ is small, it is natural to take

$$\boldsymbol{\Omega} = 2\left(\mathbf{I} + \frac{2}{\lambda^2 \Delta t}\mathbf{A}(\mathbf{w})\mathbf{V}(\lambda, \mathbf{w})^{-1}\right)^{-1}. \tag{11}$$

Let us remark that if λ is large enough then the above matrix is well defined.

In order to check practically the accuracy of the approximation, we apply the above analysis for a simplified system of two conservation laws

We consider the one-dimensional isothermal Euler equations with a diagonal diffusion of $\epsilon\partial_{xx}\left(\rho, \rho u\right)^T$. Hence the full fluid system we are interested in is given by

$$\partial_t \begin{pmatrix} \rho \\ \rho u \end{pmatrix} + \partial_x \begin{pmatrix} \rho u \\ (\rho u^2 + c^2 \rho) \end{pmatrix} = \epsilon \partial_{xx} \begin{pmatrix} \rho \\ \rho u \end{pmatrix}. \tag{12}$$

This system is a very simplified version of the MHD equation, where the magnetic field is assumed to vanish and the gas is supposed to isothermal. We have chosen to use this specific non-physical diffusion for our first test since it is exactly the type of diffusion that is apparent in a standard finite volume code using a Lax-Friedrichs flux.
The diffusion matrix for (12) is simply given by

$$\mathbf{A}(\mathbf{w}) = \begin{pmatrix} \epsilon & 0 \\ 0 & \epsilon \end{pmatrix}. \tag{13}$$

From (11), the inverse of the relaxation matrix is given by

$$\boldsymbol{\Omega}^{-1} = \begin{pmatrix} a_{1,1} & a_{1,2} \\ a_{2,1} & a_{2,2} \end{pmatrix} \tag{14}$$

with

$$a_{1,1} = \frac{\epsilon\left(\rho^4\left(\lambda^2 - c^2\right) - 3\rho^4 u^2\right)}{\Delta t\left(u^4\rho^4 + \left(c^2 - \lambda^2\right)^2\rho^4 - 2u^2\left(c^2 + \lambda^2\right)\rho^4\right)} + \frac{1}{2},$$

$$a_{1,2} = \frac{2\rho^4 u \epsilon}{\Delta t\left(u^4\rho^4 + \left(c^2 - \lambda^2\right)^2\rho^4 - 2u^2\left(c^2 + \lambda^2\right)\rho^4\right)},$$

$$a_{2,1} = -\frac{2\rho^2 u(\rho u - c\rho)(c\rho + u\rho)\epsilon}{\Delta t\left(u^4\rho^4 + \left(c^2 - \lambda^2\right)^2\rho^4 - 2u^2\left(c^2 + \lambda^2\right)\rho^4\right)},$$

$$a_{2,2} = \frac{\epsilon\left(u^2\rho^2 + \left(\lambda^2 - c^2\right)\rho^2\right)\rho^2}{\Delta t\left(u^4\rho^4 + \left(c^2 - \lambda^2\right)^2\rho^4 - 2u^2\left(c^2 + \lambda^2\right)\rho^4\right)} + \frac{1}{2}.$$

For our first test of the matrix relaxation, we solve (12) comparing the Lattice Boltzmann sheme using (11) as relaxation matrix and a standard explicit centered finite volume scheme for approximating ((12)). In this centered scheme, the time step is taken very small in such way that the stability condition is satisfied and that the time integration error can be neglected. In other words, the equivalent PDE of both schemes is (10). Hence, given the parameters in both schemes are set to represent the same diffusion ϵ, one should get the same type of diffusion for both schemes.
To test this we take the simple test case of a stationary viscous shock:
The initial data for this shock tube problem are

$$\mathrm{w}_l = (\rho_l, \rho_l u_l)^T \qquad \mathrm{w}_r = \left(\frac{\rho_l u_l^2}{c}, \frac{c}{u_l}\right)^T \tag{15}$$

where the sound speed c is set as $c = 1$ while for the left state we have chosen

$$\mathrm{w}_l = \left(2, \frac{3}{2}\right)^T. \tag{16}$$

For the diffusion we use $\epsilon = 0.1$. For the Lattice Boltzmann scheme we set $\lambda = 40$. The results on a 128 cell grid at time $T = 0.1$ are shown in Figure 1. The test shows that the matrix relaxation lattice Boltzmann scheme provides the correct diffusion and therefore results in the right viscose profile. The conclusion of this section is that the relaxation parameter is related to

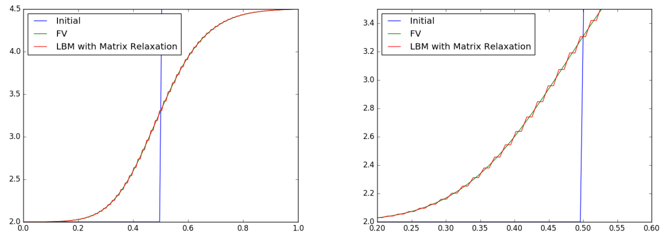

Fig. 1 Viscous Shock Test with $\epsilon = 0.1$: Comparison of the viscous profiles of the finite volume and the lattice Boltzmann scheme.

numerical viscosity. In 1D it can indeed be adjusted to fit the exact viscosity up to second order. For two-dimensional computations the analysis is more complicated, but heuristically we expect a similar behavior.

In the following, for simplicity reasons, we only consider scalar relaxation.

6 GPU implementation

We have implemented the above LBM algorithm. The LBM is particularly well adapted to parallelism. It is possible to provide very efficient implementations on GPU (Graphic Purpose Units) hardware.

6.1 OpenCL

6.1.1 Terminology

Today Graphic Processing Units (GPU) have more and more computation power. The Open Computing Language (OpenCL) is a software environment for simplifying the use of the GPUs for general computing. It is also possible to use OpenCL for driving a heterogeneous set of general multicore processors.

For giving an idea on how OpenCL is used in practice, we use the following terminology. An *accelerator* is a parallel computing device, such as a GPU or a multicore CPU. The *host* is the computer into which the accelerator is plugged. A *kernel* is a (generally small) program that is executed on several of the computing cores of the GPU. For instance, the NVidia GPU GTX470 has 448 computing cores. Thanks to the OpenCL command queue management, it is possible to launch several million kernel instances, which are dispatched on the hundreds of cores of the GPU.

OpenCL means “Open Computing Language”.

The *OpenCL runtime* is a library of C functions, called from the host, in order to drive the GPU. The OpenCL runtime, because it is written in C is quite heavy to use in practice: the verbosity is high, the API is not very user-friendly and memory management is cumbersome. For this reason it is advised to use OpenCL wrappers written in a higher-level language such as C++ or Python. We have used the Python OpenCL wrapper written by Andreas Klöckner, PyOpenCL [23], which makes OpenCL initializations and calls much easier and shorter to program.

The *OpenCL language* is a C-like language for writing the kernels that will be executed on the computing cores.

OpenCL is practically available since September 2009. The specification is managed by the Khronos Group (that also drives the OpenGL specification). Several books describe today OpenCL in detail. We can refer, for instance, to [19].

6.1.2 GPU

Very schematically we can consider that a general computing accelerator is made of *global memory* (typically 1.2 Gb for the recent NVIDIA GTX470) and *compute units* (typically 14).

Each compute unit is made of *processing elements* (typically 32), also called *processors.* A compute unit has a reserved *local memory* (typically 48 kb) shared by the processors of the unit.

A schematic picture of an abstract OpenCL accelerator is given in Figure 2

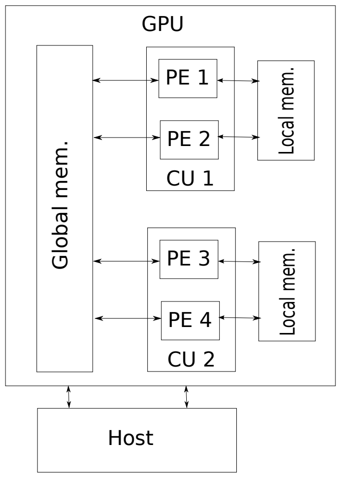

Fig. 2 A (virtual) GPU with 2 Compute Units and 4 Processing Elements

6.1.3 Programming rules

The same program can be executed on all the processing elements at the same time with the following rules:

1. All the processing elements have access to the global memory;
2. The processing elements have only access to the local memory of their compute unit;
3. The access to the global memory is relatively slow while the access to the local memory is very fast.
4. If possible, it is advised that the processing elements of the same compute unit access neighbour global memory locations, in order to improve "coalescence" (faster read/write access).

5. The memory transfers between the host memory and the GPU are slow and should be avoided;
6. If several processing elements try a read access at the same memory location (global or local) at the same time, all the reads will be successful;
7. If several processing elements try a write access at the same memory location (global or local) at the same time, ***only one write will be successful***. For some hardware, atomic operations maybe available, but should be avoided for performance reasons.

In order to perform a complex task, a kernel has to be executed many times. Each execution of a kernel is called a *work-item*. A *work-group* is a collection of work-items running on the processing elements of a given compute unit. They can access the local memory of their compute unit. Each work-item is identified by a unique global ID p.

For more details on OpenCL, we refer for instance to [19, 23].

6.2 OpenCL implementation of the LBM algorithm

We have implemented the above algorithm using PyOpenCL.

The different devices used in this paper are listed in Table 1. The AMD processor was used inside a virtual environment, which implies a non-negligible loss of performance. PyOpenCL allows to select either the CPU or the GPU for the computations. With the OpenCL AMD drivers, when the CPU is selected, it is also possible to choose the number of activated CPU cores through a Linux environment variable. This is useful for estimating (in a crude way) the efficiency of the OpenCL parallelism.

short name	name	type	frequency	memory	cache	CU	PE
V100	Tesla V100-PCIE-16GB	GPU	1.4 GHz	16 GB	48 kB	80	5120
Quadro	NVIDIA Quadro P6000	GPU	1.5 GHz	24 GB	32 kB	30	3840
GTX	NVIDIA GTX 1660	GPU	1.6 GHz	6 GB	48 kB	22	1408
AMD	AMD EPYC 7551 32-core	CPU	2 GHz	47 GB	32 kB	1-24	1-24
Intel	2 x Intel Xeon CPU E5-2609 v4	CPU	1.7 GHz	63 GB	32 kB	16	16

Table 1 Characteristics of the OpenCL devices tested in this paper. CU stands for "Compute Units" and "PE" for "Processing Elements".

The LBM is very simple. Our implementation is made of two OpenCL kernels, a few C functions and a small Python driver for initializing the memory buffers, launching the OpenCL kernel and plotting the results. The role of the first OpenCL kernel is to compute the initial condition directly into the memory buffer created on the OpenCL accelerator. The role of the second kernel is to perform a time step of the LBM. The time-stepping is driven from the PyOpenCL program.

The most important point is to take care of the organizations of the kinetic data into memory. Indeed ensuring coalescent memory access is essential for performance. In practice all the values $\mathbf{f}_{k,i,j}$ for kinetic velocities $\mathbf{v}_k$ in cells (i,j) are arranged in a single memory buffer `fn[]`, with the following storage

$$\mathbf{f}_{k,i,j} = \texttt{fn[imem]}, \quad \texttt{imem=i+j*Nx+k*Nx*Ny},$$

where `Nx` is the number of grid points in the x_1-direction and `Ny` is the number of grid points in the x_2-direction. Then, in the OpenCL kernel, each cell (i,j) is associated to the work-item

$$p = \texttt{i+j*Nx}.$$

This numbering ensures that neighboring work-items will access neighboring memory locations during the shift algorithm (5). For instance, if work-item g access data in global memory, for reading or writing, at location `imem`, then work-item $p' = p + 1$ access location `imem+1`.

This property is still true in the relaxation algorithm. First, the kinetic data are copied in processor registers in a coalescent way. The computations of the conservative data (6), equilibrium (7) and collisions (8) are done in registers, which ensure very fast memory access. Finally, the kinetic data are copied back to the global buffer `fn[]` in a fully coalescent way.

We remark that thanks to the chosen organization into memory, we do not have to use the local memory for accelerating the algorithm.

When the program is run on NVIDIA cards, monitoring tools, such as `nvtop`[1] indicates that the GPU occupation is of 99%. This indicates a quasi-optimal implementation.

7 Numerical applications to MHD

7.1 Smooth vortex (performance test)

The smooth vortex test is a classical test for MHD codes. It is described for instance in [18]. Because this is a exact solution, it allows to assess the accuracy of the solver. Here we also used this test to evaluate the efficiency of the parallel implementation. The test case is built upon a single vortex, which is a stationary solution of the MHD system, to which a constant drift velocity is added. In the moving frame centered on $\mathbf{r}_O(t) = t\mathbf{u}_{\text{drift}}$, with $\mathbf{u}_{\text{drift}} \in \mathbb{R}^2$, the analytical solution reads in polar coordinates

[1] `https://github.com/Syllo/nvtop`

$$\rho(r,\theta) = \rho_0,$$
$$\mathbf{u}(r,\theta) = u_0[\mathbf{u}_{\text{drift}} + h(r)\mathbf{e}_\theta],$$
$$\mathbf{B}(r,\theta) = b_0 h(r)\mathbf{e}_\theta,$$
$$p(r,\theta) = p_0 + \frac{b_0^2}{2}(1 - h(r)),$$

with $b_0 = \rho_0 u_0^2$. The results shown below are obtained with $\gamma = 5/3$ and the parameter set

$$\rho_0 = p_0 = 1,\ u_0 = b_0 = 0.2,\ \mathbf{u}_{\text{drift}} = (1,1)^T,\ h(r) = \exp[(1 - r^2)/2].$$

The computational domain is the square $\Omega =]-L/2, L/2[\times]L/2, L2[$, with $L = 20$. We compute the solution at time $t = 10$. The grid contains N points in x_1 and x_2 directions. For this smooth test case, we can take a relaxation parameter $\omega = 2$. We compute the error e_N in the L^1 norm at the final time between the exact solution and the numerical solution on the first component of the momentum (the other components of the solution would give similar results):

$$e_N = \int_\Omega \left|(\rho u_1)_{\text{num}} - (\rho u_1)_{\text{exact}}\right|.$$

Asymptotically, the order of the scheme is evaluated by

$$\beta \simeq \frac{\ln(e_N/e_{2N})}{\ln 2}.$$

The obtained numerical results are summed up in Table 2, where we give the convergence study and a performance evaluation of the implementation. OpenCL permits to run the same code on a multicore CPU or a GPU. We have tested several CPU or GPU hardware in single or double precision. Table 2 confirms the order of accuracy of the scheme in the case $\omega = 2$. In addition we observe a good efficiency of the implementation on several types of GPU. On CPU there is also a speedup achieved by the OpenCL parallelism, but it is very sensitive to the OpenCL drivers. For instance, with the same hardware (an Intel Xeon two-CPU system) the program runs almost three times faster with the OpenCL Intel drivers than with the open source POCL drivers. Let us finally mention that when it is run on only one core, the code is very slow. This is due to the fact that our implementation is not really optimized for harnessing correctly the CPU cache. Here, with a more clever tiling strategy, the one-core run could probably be accelerated by an order of magnitude (see for instance [21]).

	CU	precision	N=128	N=256	N=512	N=1024	"efficiency"
AMD	1	float32	11.9 s	159 s	621 s	6396 s	1
AMD	24	float32	1.01 s	9.4 s	153 s	1380 s	5
Intel (pocl)	16	float32	2.30 s	17.3 s	96.6 s	644 s	10
Intel	16	float32	0.75 s	3.93 s	32 s	226 s	30
Intel	16	float64	0.82 s	5.62 s	53 s	315 s	20
GTX	22	float32	0.04 s	0.31s	2.46 s	19.48 s	330
Quadro	30	float32	0.017 s	0.15 s	1.06 s	8.25 s	780
Quadro	30	float64	0.15 s	0.81 s	5.67 s	45.53 s	140
V100	80	float32	0.015 s	0.084 s	0.54 s	3.93 s	1600
V100	80	float64	0.031 s	0.21 s	1.17 s	8.35 s	770
e_N		float64	0.05067625	0.013039866	0.003265470	0.00081652	
β		float64	-	1.96	1.99	2.00	

Table 2 Convergence and performance study. Some tests are done in single precision (float32) and others in double precision (float64). The "efficiency" is a comparison for N=1024 with the slowest device. "CU" means "Compute Units": it is the number of activated cores in a CPU computation or of OpenCL processing elements for a GPU computation.

7.2 Orszag-Tang vortex

The Orszag-Tang test case [25, 12, 27] is often used to test a numerical method for MHD. It consists in a vortex system where turbulent structures and shocks develop. The domain is $\mathcal{D} = [0, 2\pi] \times [0, 2\pi]$ and the boundary conditions are periodic in $x_1 = x$ and $x_2 = y$. The initial conditions are given in Table 3.

Variables	States
γ	$5/3$
ρ	γ^2
p	γ
u_x	$-\sin(y)$
u_y	$\sin(x)$
u_z	0
B_x	$-\sin(y)$
B_y	$\sin(2x)$
B_z	0

Table 3 Initial states for the Orszag-Tang test case

Tilt instability

The tilt instability has been studied in [29, 30, 24]. The initial magnetic field configuration for tilt instability is a dipole current structure. It consists of

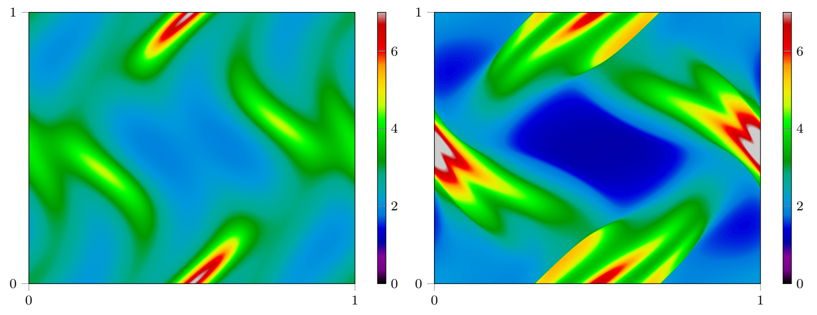

Fig. 3 Snapshots of ρ for the Orszag-Tang configuration recorded at times $t = 0.1$ s and $t = 0.2$ s. Grid size is $Nx \times Ny = 1024 \times 1024$.

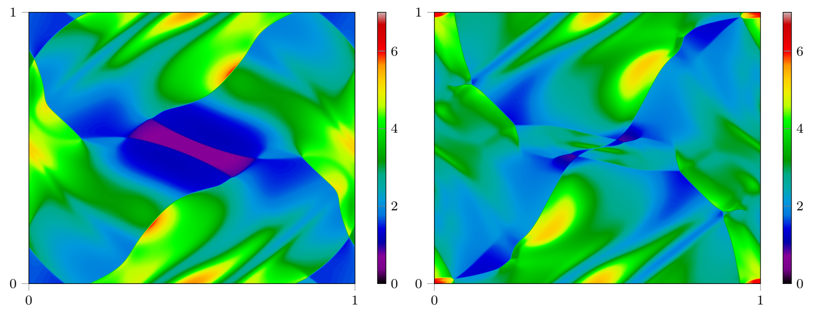

Fig. 4 Snapshots of ρ for the Orszag-Tang configuration recorded at times $t = 0.3$ s and $t = 0.4$ s. Grid size is $Nx \times Ny = 1024 \times 1024$.

two oppositely directed currents embedded in a uniform magnetic field (at large distance).

These islands may be kept in an unstable equilibrium through a strong magnetic field. However, when perturbed, an instability develops that leads the islands to be aligned horizontally and to be expelled away. The tilt instability is illustrated for a simulation on a 1024×1024 grid in Figures 6 to 8 for different times and the numerical approach presented above. A detailed description of the different stages of this instability can be found in [29, 5]. In [29, 22], the study of the tilt instability was also made for a compressible MHD system, while in [30, 24] the equations are incompressible, leading to slightly different results.

In the following, we will consider a squared spatial domain of dimensions $\mathcal{D} = [-3, 3] \times [-3, 3]$ and $r^2 = x^2 + y^2$. The initial condition for the equilibrium is given by:

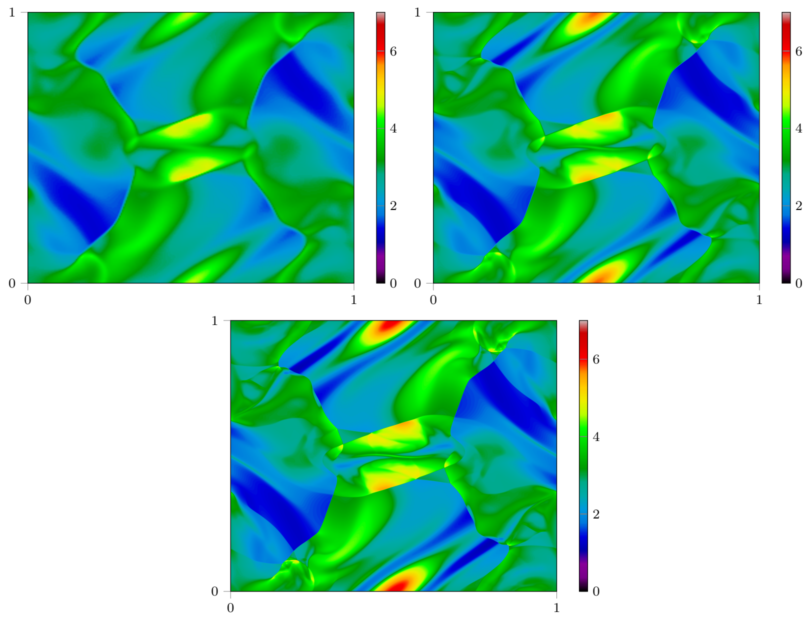

Fig. 5 Snapshots of ρ for the Orszag-Tang configuration recorded at time $t = 0.5$ s and $t = 0.2$ s. Grid sizes are $Nx \times Ny = 256 \times 256$, 1024×1024 and 4096×4096.

$$\rho = 1.0, \quad \mathbf{u} = \mathbf{0}, \quad p_0 = 1.0, \quad \psi = 0, \tag{17}$$

$$k = 3.8317059702, \quad K = \frac{-2}{kJ_0(k)}, \quad \varphi = KJ_1(kr)\frac{y}{r}, \tag{18}$$

$$p = \begin{cases} p_0 & \text{if} \quad r \geq 1, \\ p_0 + \frac{k^2}{2}\varphi^2 & \text{else,} \end{cases} \tag{19}$$

$$B_1 = \begin{cases} \frac{x^2-y^2}{r^4} - 1 & \text{if} \quad r \geq 1, \\ K\left[\frac{ky^2}{r^2}J_0(kr) + \frac{x^2-y^2}{r^3}J_1(kr)\right] & \text{else,} \end{cases} \tag{20}$$

$$B_2 = \begin{cases} \frac{2xy}{r^4} & \text{if} \quad r \geq 1, \\ -K\left[\frac{kxy}{r^2}J_0(kr) - \frac{2xy}{r^3}J_1(kr)\right] & \text{else,} \end{cases} \tag{21}$$

where J_0 and J_1 are the Bessel functions of the first kind of orders zero and one respectively. A perturbation of this equilibrium initially reads:

$$\mathbf{u} = 2\epsilon \exp\left(-r^2\right) \begin{pmatrix} -y \\ x \\ 0 \end{pmatrix},$$

with $\epsilon = 1.0 \cdot 10^{-3}$.

The asymptotic magnetic field strength for large r is unity, and thus defines our normalization. We also point out that we consider non-dimensioned equations in which the magnetic permeability is set to one. Consequently, our unit time is defined as the Alfven transit time across the unit distance (i.e. the initial characteristic length scale of the dipole structure).

Moreover, for the analysis of the simulation results, we recall that the current density is given by:

$$\mathbf{C} = \nabla \times \mathbf{B},$$

and that we are interested in the third component of $\mathbf{C}$, *i.e.* C_3. We will also look at the kinetic energy of the system, which is computed as the integral over the spatial domain of the kinetic energy density:

$$E_{\mathrm{kin}} = \int_{\mathcal{D}} \frac{1}{2}\rho|\mathbf{u}|^2.$$

We apply Dirichlet boundary conditions in this test case: the initial data in the boundary cells are simply kept constant. Finally, the numerical scheme involves the following parameters:

$$\Delta x = L_x/N_x, \quad c_h = 6 \quad \lambda = 20, \quad \Delta t = \Delta x/\lambda,$$

and $\omega = 1.9$ for all variables except from the kinetic variables associated with ψ where $\omega = 1$ (see section 7.2). In our numerical tests, we have noticed that choosing $\omega = 2$ leads to an unstable numerical solution, due to the lack of dissipation.

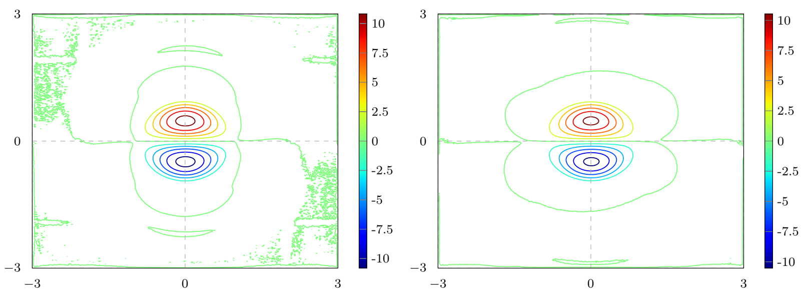

Fig. 6 Snapshots of the magnetic current density C_3 recorded at (non-dimensioned) times $t = 1$ and $t = 2$. Grid size is $Nx \times Ny = 1024 \times 1024$.

Current sheets and current peak

Current sheets develop at the edges of the magnetic islands. The width of these current sheets as well as the maximum intensity of the current den-

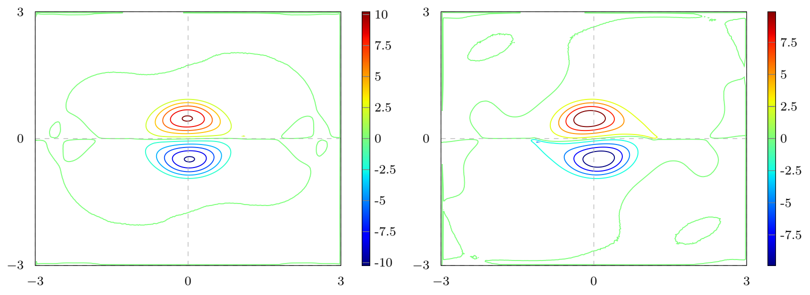

Fig. 7 Snapshots of the magnetic current density C_3 recorded at times $t = 3$ and $t = 4$. Grid size is $Nx \times Ny = 1024 \times 1024$.

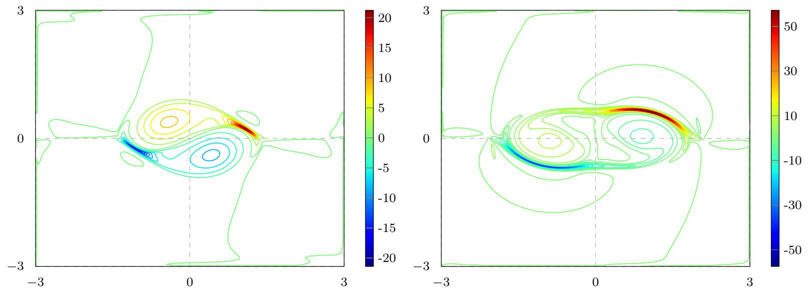

Fig. 8 Snapshots of the magnetic current density C_3 recorded at times $t = 5$ and $t = 6$. Grid size is $Nx \times Ny = 1024 \times 1024$.

sity depends on the numerical resolution, as studied in [24], where specific adaptive resolution (adaptive grid and order of resolution) was performed near strong current gradients. In Figure 9, we show an enlargement of the part of the spatial domain that lies around the current sheet lying right side for simulations with different grid sizes and at time $t = 6$. The finest current structures are obtained with the finest grid (here the 4096×4096 grid). In Figure 10, we present the ratio of the maximum current density $C_{3,max}$ over the initial current density $C_{3,0}$. This ratio increases with the numerical resolution and should be infinite in the case of a totally ideal MHD system ([24]). The maximum ratio we can obtain is 14.2 with the 7000×7000 grid. In comparison, [24] obtained a ratio of 5 for the simulation with 32,768 triangles and first-order method, and a ratio of 41 for adaptive grids near the current sheets. In conclusion, our method seems to have a higher numerical resistivity, which limits the maximum current peak, but the computations are probably faster. Indeed, adaptive methods are known to suffer from overhead due to the algorithm complexity.

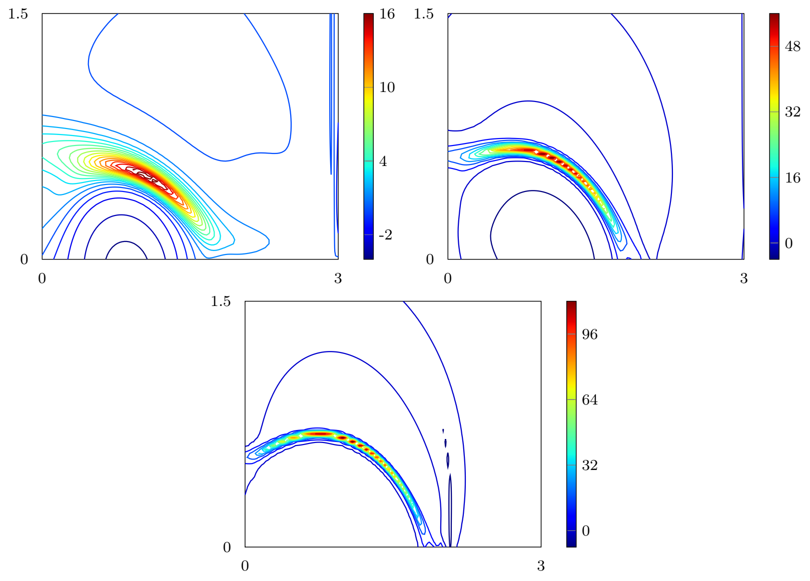

Fig. 9 Snapshots of the magnetic current density recorded at time $t = 6$ in a spatial zone around the current sheets. Grid sizes are $Nx \times Ny = 256 \times 256$, $Nx \times Ny = 1024 \times 1024$, $Nx \times Ny = 4096 \times 4096$.

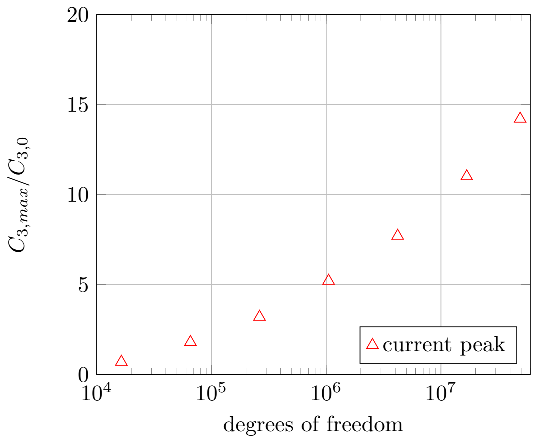

Fig. 10 Ratio of the peak current and the initial current density for simulation grids ranging from 128×128 to 7000×7000.

Kinetic energy growth rate

During the development of the instability, the kinetic energy of the system increases exponentially. The growth rate of the kinetic energy has been studied in [29] and [24], where different values have been found. In [29], two simulations with two values of β (the ratio between the hydrodynamic and the magnetic pressures) give growth rate values of 1.44 for low β case and of 1.27 for high β case. In [24], the study is focused on the convergence of the kinetic energy growth rate according to the grid and the order of the numerical method. The converged value for the growth rate is near 1.3 for an initial perturbation $\epsilon = 1.0 \cdot 10^{-3}$. In

The simulations of the tilt instability that we perform are post-processed at regular time intervals. In Figures 11 and 12, we show the time evolution of the total kinetic energy $E_{\text{kin}}(t)$. One can note that the growth of the kinetic energy happens in two stages: in a first stage, the growth is faster than exponentially, then slows down and after two seconds the second stage begins with exponential growth. When the numerical resolution is better, the first stage tends to vanish and the second stage begins sooner.

In a logarithmic scale, the linear regression of the kinetic energy growth is performed with the `Scipy` function `linregress` and the regression line is illustrated in Figures 11 and 12. The results of the linear regression are reported in Table 4 and Figure 12. The converged growth rate is close to 1.45 for our simulations. It is higher than the results of [29] and [24]. In [22] for a similar configuration the growth rate is evaluated to 1.498. This probably very close to the exact rate because the simulation is conducted with a very precise adaptive scheme. Our results seem thus to be quite precise on the finest mesh.

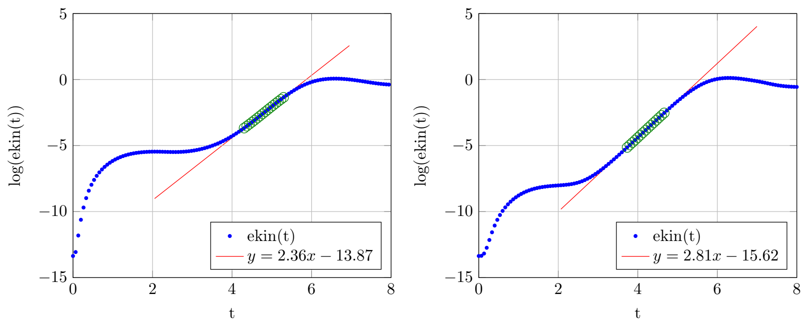

Fig. 11 Growth of the kinetic energy during the simulation. Measures that have been accounted for the linear regression are identified with green marks and the regression line is in red. Results for grid sizes $Nx \times Ny = 512 \times 512$ and $Nx \times Ny = 2048 \times 2048$.

In Table 4, we summarize the characteristics of the linear regression for each mesh size.

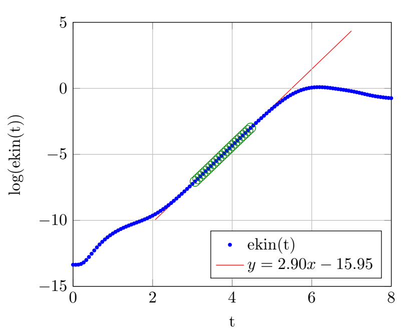

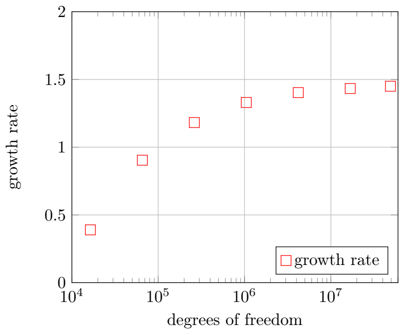

Fig. 12 Growth of the kinetic energy during the simulation. Measures that have been accounted for the linear regression are identified with green marks and the regression line is in red. Results for grid size $Nx \times Ny = 7000 \times 7000$. Growth rates from $Nx = Ny = 128$ (16384 degrees of freedom) to $Nx = Ny = 7000$ (49×10^6 degrees of freedom).

Mesh size	128^2	256^2	512^2	1024^2	2048^2	4096^2	7000^2
Regression range (s)	$[5.6, 6.7]$	$[4.9, 5.9]$	$[4.3, 5.3]$	$[3.9, 4.9]$	$[3.7, 4.7]$	$[3.0, 4.5]$	$[3.0, 4.5]$
Growth rate	0.390	0.904	1.082	1.330	1.403	1.433	1.450

Table 4 Characteristics of the linear regression for the kinetic energy growth rate for each mesh size: range of values that have been accounted for and growth rate.

Divergence cleaning effect

In order to ensure a magnetic field which is close to a divergence-free field, we have presented the divergence cleaning procedure in Section 2.1. Here we compare two strategies for the numerical resolution of the divergence cleaning equation:

1. the kinetic variables associated with the macro-variable ψ are solved numerically like any other kinetic variable. This means that in the relaxation step, the relaxation coefficient ω is set to $\omega = 1.9$ and the order of resolution is close to 2,
2. during the relaxation step, the kinetic variables associated with the macro-variable ψ are relaxed with a coefficient $\omega = 1$, which comes down to set

$$\begin{aligned}\mathbf{f}_{k,i,j}^{n+1} &= \omega \mathbf{f}_k^{eq}(\mathbf{w}_{i,j}^{n+1}) - (\omega - 1)\mathbf{f}_{k,i,j}^{n+1,-} \\ &= \mathbf{f}_k^{eq}(\mathbf{w}_{i,j}^{n+1}).\end{aligned}$$

Now, the order of resolution is 1 and the waves associated with the perturbations of the divergence-free constraint are better damped than with $\omega = 1.9$. In [13], several strategies are proposed for damping the divergence errors. One of the methods is to introduce a viscous damping term. In its spirit our proposal is similar, but the viscous term is introduced here in a numerical way.

These two options are compared in Figures 13 to 15 for different times. At time $t = 0.5$ s, one can notice the effects of the boundary conditions that have propagated towards the center of the domain. The perturbations of the divergence-free constraint have been more attenuated with the second strategy than with the first one. At time $t = 1$ s, the divergence-free constraint is mainly violated at the edges of the magnetic vortices and close to the domain boundaries. Once more, the results are better with the second divergence cleaning strategy. Finally, at time $t = 5$ s, when the vortices have begun to align, the divergence-free constraint is strongly perturbed, but results are still better with the second strategy.

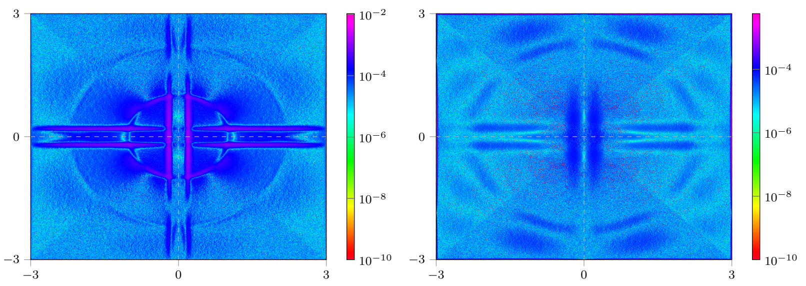

Fig. 13 Snapshots of the divergence of the magnetic field recorded at times $t = 0.5$ s for both strategies of divergence cleaning. Grid size is $Nx \times Ny = 1024 \times 1024$.

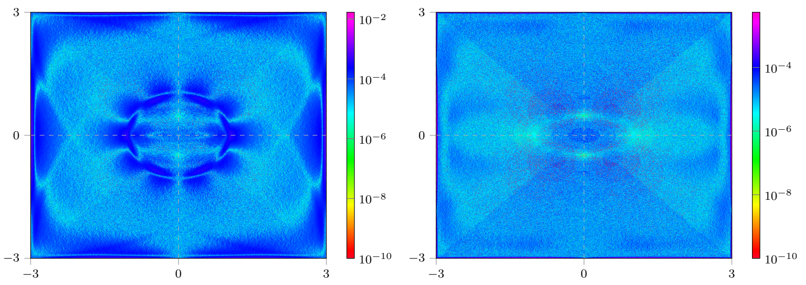

Fig. 14 Snapshots of the divergence of the magnetic field recorded at times $t = 1$ s for both strategies of divergence cleaning. Grid size is $Nx \times Ny = 1024 \times 1024$.

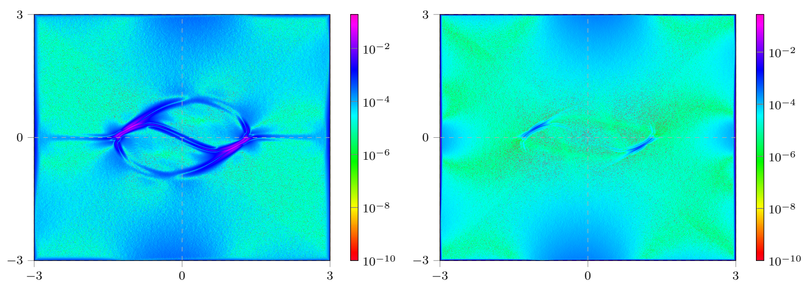

Fig. 15 Snapshots of the divergence of the magnetic field recorded at times $t = 5$ s for both strategies of divergence cleaning. Grid size is $Nx \times Ny = 1024 \times 1024$.

8 Conclusion

In this work we have proposed a fast and robust Lattice-Boltzmann solver for the two-dimensional MHD equations with divergence cleaning. The method is general and can be extended to other systems of conservation laws.

We have provided a preliminary one-dimensional analysis in order to evaluate the numerical viscosity of the numerical scheme. We have shown that in principle, the numerical viscosity can be adjusted to a specific viscosity. An interesting challenge would be to extend the analysis to higher dimensions, but this leads to complex calculations because of cross second-order derivatives. If this analysis is possible, this would lead to a scheme where the physical resistive terms could be approximated properly.

The kinetic representation of the equations is very well adapted to massive parallel computing. The simplicity of the algorithm allows achieving almost optimal efficiency on GPU hardware. This leads to the possibility to conduct computations on very fine uniformly refined meshes.

When conducting the simulations, we observed that the limiting factor was memory rather than computation time. In order to extend the method to even finer meshes or to three-dimensional computations, the memory management has to be improved. An obvious possibility is to distribute the computations on several GPUs, using a task-based runtime system (such as in [7]). This approach could also be mixed with a compression strategy in order to reduce memory occupation and data transfers.

References

1. Denise Aregba-Driollet and Roberto Natalini. Discrete kinetic schemes for multi-dimensional systems of conservation laws. *SIAM Journal on Numerical Analysis*, 37(6):1973–2004, 2000.
2. Jayesh Badwaik, Matthieu Boileau, David Coulette, Emmanuel Franck, Philippe Helluy, Christian Klingenberg, Laura Mendoza, and Herbert Oberlin. Task-based paral-

lelization of an implicit kinetic scheme. *ESAIM: Proceedings and Surveys*, 63:60–77, 2018.

3. Jayesh Badwaik, Matthieu Boileau, David Coulette, Emmanuel Franck, Philippe Helluy, Laura Mendoza, and Herbert Oberlin. Task-based parallelization of an implicit kinetic scheme. https://hal.archives-ouvertes.fr/hal-01451393, January 2017.
4. Timothy Barth. On the role of involutions in the discontinuous galerkin discretization of maxwell and magnetohydrodynamic systems. In *Compatible spatial discretizations*, pages 69–88. Springer, 2006.
5. Hubert Baty. Finmhd: An adaptive finite-element code for magnetic reconnection and formation of plasmoid chains in magnetohydrodynamics. *The Astrophysical Journal Supplement Series*, 243(2):23, 2019.
6. François Bouchut. Construction of BGK models with a family of kinetic entropies for a given system of conservation laws. *Journal of Statistical Physics*, 95(1-2):113–170, 1999.
7. Bérenger Bramas, Philippe Helluy, Laura Mendoza, and Bruno Weber. Optimization of a discontinuous galerkin solver with opencl and starpu. *International Journal on Finite Volumes*, 15(1):1–19, 2020.
8. Shiyi Chen and Gary D Doolen. Lattice boltzmann method for fluid flows. *Annual review of fluid mechanics*, 30(1):329–364, 1998.
9. David Coulette, Emmanuel Franck, Philippe Helluy, Michel Mehrenberger, and Laurent Navoret. *Palindromic Discontinuous Galerkin Method*, pages 171–178. Springer International Publishing, Cham, 2017.
10. David Coulette, Emmanuel Franck, Philippe Helluy, Michel Mehrenberger, and Laurent Navoret. High-order implicit palindromic discontinuous galerkin method for kinetic-relaxation approximation. *Computers & Fluids*, 190:485–502, 2019.
11. Clémentine Courtès, David Coulette, Emmanuel Franck, and Laurent Navoret. Vectorial kinetic relaxation model with central velocity. application to implicit relaxations schemes. *Communications in Computational Physics*, 27(4), 2020.
12. R. B. Dahlburg and J. M. Picone. Evolution of the orszag-tang vortex system in a compressible medium. i. initial average subsonic flow. *Physics of Fluids B: Plasma Physics*, 1(11), 1989.
13. Andreas Dedner, Friedemann Kemm, Dietmar Kröner, C-D Munz, Thomas Schnitzer, and Matthias Wesenberg. Hyperbolic divergence cleaning for the mhd equations. *Journal of Computational Physics*, 175(2):645–673, 2002.
14. Paul J Dellar. Lattice kinetic schemes for magnetohydrodynamics. *Journal of Computational Physics*, 179(1):95–126, 2002.
15. Paul J Dellar. An interpretation and derivation of the lattice boltzmann method using strang splitting. *Computers & Mathematics with Applications*, 65(2):129–141, 2013.
16. Florence Drui, Emmanuel Franck, Philippe Helluy, and Laurent Navoret. An analysis of over-relaxation in a kinetic approximation of systems of conservation laws. *Comptes Rendus Mécanique*, 347(3):259–269, 2019.
17. François Dubois. Equivalent partial differential equations of a lattice boltzmann scheme. *Computers & Mathematics with Applications*, 55(7):1441–1449, 2008.
18. Michael Dumbser and Raphaël Loubère. A simple robust and accurate a posteriori sub-cell finite volume limiter for the discontinuous galerkin method on unstructured meshes. *Journal of Computational Physics*, 319:163 – 199, 2016.
19. Benedict Gaster, Lee Howes, David R Kaeli, Perhaad Mistry, and Dana Schaa. *Heterogeneous computing with openCL: revised openCL 1.* Newnes, 2012.
20. Benjamin Graille. Approximation of mono-dimensional hyperbolic systems: A lattice Boltzmann scheme as a relaxation method. *Journal of Computational Physics*, 266:74–88, 2014.
21. Philippe Helluy, Thomas Strub, Michel Massaro, and Malcolm Roberts. Asynchronous opencl/mpi numerical simulations of conservation laws. In *Software for Exascale Computing-SPPEXA 2013-2015*, pages 547–565. Springer, 2016.

22. Rony Keppens, Oliver Porth, and Chun Xia. Interacting tilt and kink instabilities in repelling current channels. *The Astrophysical Journal*, 795(1):77, 2014.
23. Andreas Klöckner, Nicolas Pinto, Yunsup Lee, Bryan Catanzaro, Paul Ivanov, and Ahmed Fasih. Pycuda and pyopencl: A scripting-based approach to gpu run-time code generation. *Parallel Computing*, 38(3):157–174, 2012.
24. Shrinivas Lankalapalli, Joseph E Flaherty, Mark S Shephard, and Hank Strauss. An adaptive finite element method for magnetohydrodynamics. *Journal of Computational Physics*, 225(1):363–381, 2007.
25. Steven A Orszag and Cha-Mei Tang. Small-scale structure of two-dimensional magnetohydrodynamic turbulence. *Journal of Fluid Mechanics*, 90(1):129–143, 1979.
26. Hiroshi Otomo, Bruce M Boghosian, and François Dubois. Two complementary lattice-boltzmann-based analyses for nonlinear systems. *Physica A: Statistical Mechanics and its Applications*, 486:1000–1011, 2017.
27. J. M. Picone and R. B. Dahlburg. Evolution of the orszag-tang vortex system in a compressible medium. ii. supersonic flow. *Physics of Fluids B: Plasma Physics*, 3(29), 1991.
28. K. G. Powell. An approximate Riemann solver for magnetohydrodynamics (that works in more than one space dimension. Technical Report NASA/CR-194902 ICASE Report No. 94-24, ICASE-NASA Langley, ICASE, NASA Langley Research Center, April 1994.
29. R. L. Richard, R. D. Sydora, and M. Ashour-Abdalla. Magnetic reconnection driven by current repulsion. *Physics of Fluids B: Plasma Physics*, 2(3):488–494, 1990.
30. H.R. Strauss and D.W. Longcope. An adaptive finite element method for magnetohydrodynamics. *Journal of Computational Physics*, 147(2):318 – 336, 1998.
31. Sauro Succi. *The lattice Boltzmann equation: for fluid dynamics and beyond*. Oxford university press, 2001.